J. Fluid Mech. (2014), *vol.* 745, *pp.* 592–620.
doi:10.1017/jfm.2014.76

Fluid injection into a confined porous layer

Samuel S. Pegler[1,†], Herbert E. Huppert[1,2,3] and Jerome A. Neufeld[1,4]

[1]Institute of Theoretical Geophysics, Department of Applied Mathematics and Theoretical Physics, University of Cambridge, Wilberforce Road, Cambridge CB3 0WA, UK

[2]Faculty of Science, University of Bristol, Bristol BS8 1UH, UK

[3]School of Mathematics and Statistics, University of New South Wales, Sydney, NSW 2052, Australia

[4]BP Institute and Department of Earth Sciences, Bullard Laboratories, University of Cambridge, Madingley Road, Cambridge CB3 0EZ, UK

(Received 6 October 2013; revised 20 January 2014; accepted 31 January 2014; first published online 24 March 2014)

We present a theoretical and experimental study of viscous flows injected into a porous medium that is confined vertically by horizontal impermeable boundaries and filled with an ambient fluid of different density and viscosity. General three-dimensional equations describing such flows are developed, showing that the dynamics can be affected by two separate contributions: spreading due to gradients in hydrostatic pressure, and that due to the pressure drop introduced by the injection. In the illustrative case of a two-dimensional injection of fluid at a constant volumetric rate, the injected fluid initially forms a viscous gravity current insensitive both to the depth of the medium and to the viscosity of the ambient fluid. Beyond a characteristic time scale, the dynamics transition to being dominated by the injection pressure, and the injected fluid eventually intersects the second boundary to form a second moving contact line. Three different late-time asymptotic regimes can emerge, depending on whether the viscosity of the injected fluid is less than, equal to or greater than that of the ambient fluid. With a less viscous injection, the flow undergoes a slow decay towards a similarity solution in which the two contact lines extend linearly in time with differing prefactors. Perturbations from this long-term state are shown to decay algebraically with time. Equal viscosities result in both contact lines approaching the same leading-order asymptotic position but with a first-order correction to the distance between them that expands as $t^{1/2}$ due to gravitational spreading. For a more viscous injection, the distance between the contact lines approaches a constant value, with perturbations decaying exponentially. Data from a new series of laboratory experiments confirm these theoretical predictions.

Key words: geophysical and geological flows, gravity currents, porous media

1. Introduction

Gravity currents in porous media occur frequently within geological, environmental and industrial settings. Many theoretical studies of such flows have focused on those cases in which the current flows along a rigid boundary in a porous medium that

† Email address for correspondence: ssp23@cam.ac.uk

is unconfined or idealized as infinitely deep (Huppert 1986; Bear 1988; Huppert & Woods 1995; Barenblatt 1996; Lyle *et al.* 2005; Vella & Huppert 2006; Golding & Huppert 2010; Pegler, Huppert & Neufeld 2013*a*). However, there are important situations where the medium is confined by a second horizontal boundary. Our interest stems mainly from the application to the emerging technology of carbon capture and storage (CCS), where carbon dioxide (CO_2) is injected at high pressures into confined aquifers deep underground (Orr 2009). At the In Salah test site in Algeria, CO_2 is injected roughly 2 km into a porous sandstone layer containing ambient salt water, forming a relatively shallow porous layer with a typical thickness of about 20 m through which the injected current of CO_2 flows (Vasco *et al.* 2010).

Previous theoretical studies of flows in confined porous media (e.g. Bear 1988; Huppert & Woods 1995; Nordbotten & Celia 2006; Hesse *et al.* 2007; MacMinn & Juanes 2009; Gunn & Woods 2011) have revealed that confinement introduces fundamentally new dynamics compared to those that apply in unconfined porous media. While flows in unconfined media can be modelled to leading order as being driven purely by gradients in buoyancy (Huppert & Woods 1995), the constraint on the total thickness of flows in confined porous media implies that they are subject to additional pressure gradients associated with driving the fluids horizontally along the length of the medium. Such *background* pressure gradients, caused for example by the pressure drop between a point of injection and the far field of the medium, have the potential to independently drive flows in confined porous layers. A further aspect of confinement relates to the contact between the injected current and the underlying boundary, which partitions the flow at a moving contact line between a region spanning the depth of the medium and a region containing the interface between the fluids. This moving contact line is analogous to that which arises in studies of shear-dominated viscous flows that are separated between a floating and a grounded component (Pegler *et al.* 2013*b*).

Within the context of CCS, there is the potential for the gradients in buoyancy or background pressure arising from vertical confinement to be significant in controlling the flow of CO_2. This has been illustrated previously in the context of an idealized axisymmetric injection (Nordbotten & Celia 2006). Our focus in this paper is to elucidate for the first time general conditions that determine which of these gradients is the more significant driving force, and to analyse the fluid-mechanical regimes that can occur when a fluid is injected into an idealized two-dimensional horizontal porous layer.

Early analysis of flows in confined porous layers considered the exchange flows between aquifers filled with fluids of equal viscosities but different densities (Bear 1988; Huppert & Woods 1995). By applying thin-layer approximations, these authors analysed the predominantly horizontal flow, showing that it can be described by a similarity solution exhibiting a linear interface between the fluid layers. Nordbotten & Celia (2006) allowed for different viscosities between the two fluid layers in the context of an axisymmetric injection, showing that such flows can be described by a class of similarity solutions in which the relative significance of buoyancy- and injection-driven flow remain equal over time. Transient flows in confined porous media have been studied in the context of a two-dimensional finite-volume release by Hesse *et al.* (2007), who showed that the purely buoyancy-driven flow undergoes a transition from an early-time self-similar exchange flow towards a late-time regime equivalent to that which applies in unconfined or infinitely deep porous layers. Other recent analysis has focused on the effects of different initial conditions, capillary trapping, inclination and background flow (Hesse, Orr & Tchelepi 2008; MacMinn & Juanes 2009; MacMinn, Szulczewski & Juanes 2010, 2011; Gunn & Woods 2011, 2012).

We extend these earlier studies by considering the two-dimensional injection of a fluid into a horizontal medium at a constant flux from an idealized line source. The primary aim of our analysis is to model both the pressure gradients due to injection and those due to buoyancy simultaneously, thus building on the analysis of Hesse *et al.* (2007) to allow for the pressure gradients associated with the injection, and that of Gunn & Woods (2011) by including gradients in buoyancy. Unlike the self-similar solutions that can be used to describe all instances of an axisymmetric injection (Nordbotten & Celia 2006), a two-dimensional injection undergoes transitions that connect the regimes governed by gravitational spreading to those driven primarily by the injection pressure. In our theoretical development, we begin by establishing the general three-dimensional equations describing flows in confined porous layers, which we use to elucidate how the dynamics can generally be separated into those that involve gravitational spreading and those associated with the pressurization of the fluid at the injection. We subsequently describe the different two-dimensional flow regimes that occur between cases in which the injected fluid is of larger, the same or smaller viscosity than the ambient fluid. In the last two of these, we show how the flows have as long-term limits the similarity solutions obtained by Huppert & Woods (1995) and Gunn & Woods (2011), with our analysis elucidating the conditions and scales on which these transitions occur. We also reveal the new asymptotic regimes that emerge when the injected fluid is more viscous than the ambient fluid.

Experimental analysis of shallow flows in porous media has to date concentrated on gravity-driven flow in unconfined porous media (Huppert & Woods 1995; Woods & Mason 2000; Lyle *et al.* 2005; Vella & Huppert 2006; Golding & Huppert 2010; Pegler *et al.* 2013*a*). Here, we present new laboratory experiments of flows in confined porous layers, thus providing a benchmark against which to compare our theoretical predictions.

We begin in § 2 by deriving the general equations describing three-dimensional thin-layer flows in confined porous media. In § 3, we analyse the two-dimensional injection due to a line source, describing the transitions between early- and late-time asymptotic regimes. In § 4, we present our laboratory study and discuss the comparison between the experimental data and our theoretical predictions. In § 5 we apply our theoretical results to assess the importance of injection-driven flow in some illustrative geophysical settings, before summarizing our conclusions in § 6.

2. Theoretical model

Consider a viscous fluid of viscosity μ_c and density ρ_c flowing above an ambient fluid of viscosity μ_a and larger density $\rho_a > \rho_c$ in a porous medium of uniform permeability k and porosity ϕ (see figure 1). We assume that the medium is confined vertically by horizontal boundaries along $z = 0$ and $z = H$, and that the two fluid layers are separated at all times by a sharp interface $z = h(\boldsymbol{x}, t)$, where $\boldsymbol{x} \equiv (x, y)$. Applying Darcy's law, we assume that the horizontal and vertical Darcy velocities of each layer, denoted $\boldsymbol{u}_i \equiv (u_i, v_i)$ and w_i, respectively, satisfy

$$\boldsymbol{u}_i = -\lambda_i \boldsymbol{\nabla} p_i, \quad w_i = \lambda_i \left[-\frac{\partial p_i}{\partial z} + \rho_i g \right], \quad \frac{\partial w_i}{\partial z} + \boldsymbol{\nabla} \cdot \boldsymbol{u}_i = 0, \tag{2.1a,b,c}$$

respectively, where $\boldsymbol{\nabla}$ is the horizontal gradient operator, g is the acceleration due to gravity, $\lambda_i \equiv k/\mu_i$ is the *mobility* and the subscript i denotes either c or a (Bear 1988). A scaling between the terms in the continuity equation (2.1*c*) indicates that $w_i/u_i \sim$

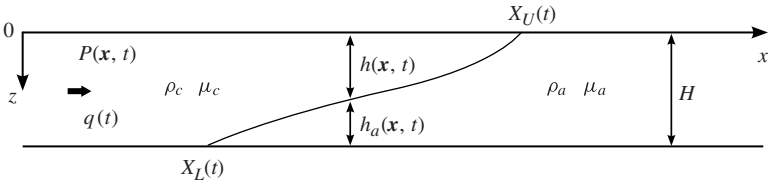

FIGURE 1. Cross-section of two fluid layers flowing in a porous medium confined between horizontal boundaries along $z = 0$ and $z = H$.

H/L, where L is a characteristic horizontal length scale of the flow. Thus, if the flow is much longer than it is deep ($L \gg H$), as is characteristic of many flows in aquifers (Bear 1988), then $w_i \sim (H/L)u_i \ll u_i$ and the flow is predominately horizontal. Under this approximation, the vertical velocity w_i can be neglected to leading order in (2.1*b*), thus yielding a purely hydrostatic vertical force balance (Bear 1988). Integrating the resulting form of (2.1*b*) and applying the continuity of pressure ($p_c = p_a$) along the interface ($z = h$), we determine the leading-order pressures in the upper and lower layers as

$$p_c = P(\boldsymbol{x}, t) + \rho_c g z \qquad (0 < z < h), \tag{2.2a}$$

$$p_a = P(\boldsymbol{x}, t) - \Delta\rho g h + \rho_a g z \qquad (h < z < H), \tag{2.2b}$$

respectively, where $\Delta\rho \equiv \rho_a - \rho_c$ is the density difference and $P(\boldsymbol{x}, t) \equiv p(\boldsymbol{x}, 0, t)$ is the unknown two-dimensional *background pressure* along the top boundary of the medium. Substituting (2.2*a,b*) into (2.1*a*) for both fluid layers ($i = c$ and a), we determine their horizontal velocities as

$$\boldsymbol{u}_c = -\lambda_c \nabla P \qquad (0 < z < h), \tag{2.3a}$$

$$\boldsymbol{u}_a = -\lambda_a \nabla [P - \Delta\rho g h] \qquad (h < z < H), \tag{2.3b}$$

which differ owing to the different mobilities λ_c and λ_a acting as prefactors to ∇P, and to the action of buoyancy due to the density difference $\Delta\rho$.

Integrating the continuity equation (2.1*c*) vertically across the depth of the upper fluid and across the full depth of the aquifer, we obtain the two equations

$$\phi \frac{\partial h}{\partial t} + \nabla \cdot (h\boldsymbol{u}) = 0, \qquad \nabla \cdot [h\boldsymbol{u} + h_a \boldsymbol{u}_a] = 0, \tag{2.4a,b}$$

respectively, where $h_a \equiv H - h$ is the thickness of the lower fluid layer below the interface, and we have dropped the c subscript for denoting quantities associated with the upper fluid. Equation (2.4*a*) represents conservation of mass in the upper fluid layer, while (2.4*b*) represents conservation of the total mass of both layers. Substituting (2.3*a,b*) into (2.4*a,b*), we obtain the governing equations

$$\phi \frac{\partial h}{\partial t} - \lambda \nabla \cdot [h \nabla P] = 0, \tag{2.5}$$

$$\nabla \cdot [(\lambda h + \lambda_a h_a) \nabla P - \Delta\rho g \lambda_a h_a \nabla h] = 0, \tag{2.6}$$

which form a coupled hyperbolic–elliptic system. Given the position of the interface $h(\boldsymbol{x}, t)$ at a point in time, (2.6) can be solved as an elliptic boundary-value problem

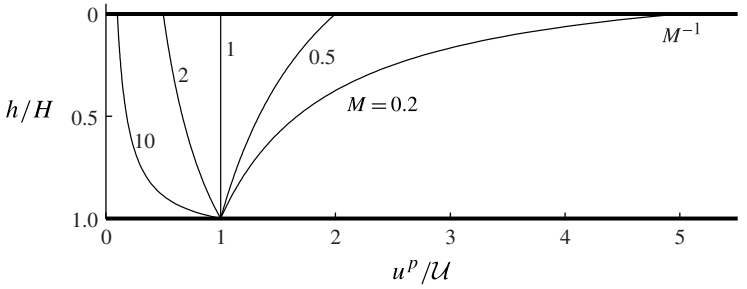

FIGURE 2. The contribution to the rate of flow of the upper layer due to the gradients in background pressure u^p, defined in (2.10), scaled by the natural velocity (3.3*c*), plotted against the dimensionless height of the interface h/H for a selection of mobility ratios M. The plot illustrates how u^p either increases or decreases from unity when the interface lies on the lower boundary ($h = H$) to M^{-1} when the interface lies on the top boundary ($h = 0$), depending on whether M is less than or greater than unity.

for the background pressure P. Once P is obtained, the hyperbolic equation (2.5) can be used to evaluate the evolution of the interface h. The elliptic nature of the integration of (2.6) for P implies that the dynamics of flows in confined porous media generally depend on a global force balance throughout the medium, with potentially long-range influences and sensitivity to far-field details. These can be contrasted with the local character of the force balance between buoyancy and viscous stresses governing gravity currents in unconfined porous media.

Generally, the interface between the two fluids will lie between two contact lines $\boldsymbol{x} = \boldsymbol{X}_U(t)$ and $\boldsymbol{X}_L(t)$ along the upper and lower boundaries, respectively. To model their propagation, we impose

$$h = 0, \quad \phi\dot{\boldsymbol{X}}_U = \boldsymbol{u} = -\lambda\boldsymbol{\nabla}P \qquad (\boldsymbol{x} = \boldsymbol{X}_U), \tag{2.7a,b}$$

$$h = H, \quad \phi\dot{\boldsymbol{X}}_L = \boldsymbol{u}_a = -\lambda_a\boldsymbol{\nabla}[P - \Delta\rho g h] \quad (\boldsymbol{x} = \boldsymbol{X}_L), \tag{2.8a,b}$$

where we have used an overdot to denote $\mathrm{d}/\mathrm{d}t$. The conditions of vanishing thickness, (2.7*a*) and (2.8*a*), follow from the continuity of the depth-integrated forms of the pressures (2.2*a,b*). The equations describing the rates of propagation of the contact lines, (2.7*b*) and (2.8*b*), follow from an application of local mass conservation at each contact line.

2.1. *Two-dimensional flow*

If the flow is idealized as two-dimensional, with no variation across its width ($\partial/\partial y = 0$), then the continuity equation (2.6) can be integrated to yield

$$hu + h_a u_a = -(\lambda h + \lambda_a h_a)\frac{\partial P}{\partial x} + \Delta\rho g \lambda_a h_a \frac{\partial h}{\partial x} = q(t), \tag{2.9}$$

where $q(t)$ is the 'constant' of integration representing the volumetric flux per unit width along the length of the aquifer (Bear 1988; Huppert & Woods 1995; Gunn & Woods 2011). Among the three-dimensional flows described by the general equations (2.5) and (2.6), those that are idealized as two-dimensional or axisymmetric share a unique property represented by (2.9) and its axisymmetric analogue (Nordbotten &

Celia 2006), namely, that the background pressure P can be related locally to the interface position h. This contrasts with the generally global dependence on h implied by the elliptic equation (2.6), where the freedom for flow in the y-direction generally precludes an exact integration. In special cases where no fluid enters or leaves the medium, a similar equation to (2.9) applies but with $q(t)$ identically equal to zero (Hesse *et al.* 2007).

Using (2.9) to evaluate $\partial P/\partial x$ in (2.5), we obtain the horizontal velocities of the upper and lower layers as

$$u = u^p + u^g \equiv \frac{q(t)}{h + Mh_a} + \frac{-MUh_a}{h + Mh_a}\frac{\partial h}{\partial x}, \tag{2.10}$$

$$u_a = u_a^p + u_a^g \equiv \frac{Mq(t)}{h + Mh_a} + \frac{MUh}{h + Mh_a}\frac{\partial h}{\partial x}, \tag{2.11}$$

respectively, where

$$U \equiv \Delta\rho g\lambda, \quad M \equiv \frac{\lambda_a}{\lambda} \equiv \frac{\mu}{\mu_a} \tag{2.12a,b}$$

are the natural buoyancy velocity of the upper layer and the mobility ratio, respectively. In (2.10) and (2.11), we have separated the velocities u and u_a into two contributions: that which is driven by the background pressure gradient u^p; and that which is driven by the local hydrostatic buoyancy gradient u^g. The contributions due to u^g and u_a^g are proportional to the slope of the interface $\partial h/\partial x$, in common with gravity currents in unconfined media. The contributions due to u^p and u_a^p depend only on the position of the interface h. This reflects the fact that the partitioning of the action of the background pressure gradient between the upper and lower fluid layers is dependent on the relative thicknesses of the layers. When $M < 1$, for example, the contribution to the flow rate due to the background pressure u_p increases as h decreases because the flow prefers the path of least resistance (see figure 2). The velocities in (2.10) and (2.11) can be related to one another through the relationships

$$u_a^p = Mu^p, \quad u_a^g = -(h/h_a)u^g. \tag{2.13a,b}$$

Equation (2.13*a*) shows that, at any location of x, the background pressure drives the fluid layers in the same direction at rates that depend on the ratio of the viscosities between the layers M. The relationship between the contributions due to buoyancy (2.13*b*) shows that it drives the fluid layers in opposite directions, reflecting the equal and opposite action of buoyancy along a fluid interface.

Substitution of (2.10) into the two-dimensional form of the continuity equation (2.4*a*) determines the nonlinear diffusion equation governing the evolution of the interface,

$$\phi\frac{\partial h}{\partial t} + \frac{\partial}{\partial x}[h\{u^p + u^g\}] = \phi\frac{\partial h}{\partial t} + \frac{\partial}{\partial x}\left[\frac{h\left\{q(t) - MUh_a\dfrac{\partial h}{\partial x}\right\}}{h + Mh_a}\right] = 0, \tag{2.14}$$

which generalizes the model developed by Huppert & Woods (1995) to accommodate variations in viscosity ($M \neq 1$) and that of Hesse *et al.* (2007) to accommodate the flux due to the injection pressure. Equation (2.14) is the two-dimensional analogue of that analysed by Nordbotten & Celia (2006) (their equation (8)). In contrast to general

three-dimensional flows, for which the full elliptic–hyperbolic system (2.5) and (2.6) must be considered, two-dimensional flows can be described by the single parabolic equation (2.14).

Depending on the relative magnitude of the velocity due to the background pressure gradient u^p compared to that due to the buoyancy gradient u^g, (2.14) can exhibit either parabolic or purely hyperbolic character. We compare the contributions of gravity-driven spreading to background-pressure-driven spreading by defining their ratio

$$G(x,t) \equiv \frac{u^g}{u^p} \equiv \frac{-MUh_a\dfrac{\partial h}{\partial x}}{q(t)}. \tag{2.15}$$

Studies of unconfined aquifers have shown that, when the flow is driven by gravity alone ($G \gg 1$), the flux satisfies the scaling relationship $q \sim hu^g \sim -Uh\,\partial h/\partial x$. Substitution of this scale for q into (2.15) yields the quantity

$$\widetilde{G}(x,t) \equiv Mh_a/h \sim MH/h. \tag{2.16}$$

This quantity characterizes the significance of gravitational spreading compared to that driven by the background pressure. Because of its association with the vertical confinement of the flow, one might expect the background-pressure-driven contribution u^p to be significant only when the depth of the current is comparable to that of the aquifer ($h \sim H$). However, this is incorrect if the injected fluid is much less viscous than the ambient fluid, $M \ll 1$, where the weaker condition $h \sim MH$, stating that the depth of the current is comparable to the product of the mobility ratio and the depth of the aquifer, implies that $\widetilde{G} = O(1)$ and is therefore sufficient to imply the significance of these pressure gradients. With the value $M \approx 0.1$ relevant to CCS (see § 5), for example, the confinement of the flow can be expected to play a role if the depth of the current spans just 10 % of the aquifer.

3. Injection at a line source

While the theoretical results above are applicable for a time-dependent flux $q(t)$, we proceed to consider the illustrative example in which fluid is injected into the medium at a constant rate. To specify the injection, we impose

$$q = hu = h\left(\frac{q_0 - MUh_a\dfrac{\partial h}{\partial x}}{h + Mh_a}\right) = q_0 \quad (x = 0), \tag{3.1}$$

with constant q_0, which can be satisfied if either

$$-Uh\frac{\partial h}{\partial x} = q_0 \quad \text{or} \quad h_a = 0 \quad (x = 0). \tag{3.2a,b}$$

The former provides a condition on the gradient of the interface $\partial h/\partial x$ at the source and is mathematically identical to that which is applied in models of two-dimensional gravity currents in unconfined porous layers (Pegler *et al.* 2013*a*). The equivalence follows from the fact that, when combined with (2.11), the condition (3.1) implies that the ambient fluid is locally stagnant ($u_a = 0$) at $x = 0$, so the local flow at that location

satisfies the conditions that can be applied uniformly to leading order throughout flows in unconfined porous media. Here, we impose condition (3.2*a*) only before the current spans the depth of the aquifer (while $h_a > 0$). Once $h_a = 0$, condition (3.2*a*) is no longer applicable because the interface is no longer located at $x = 0$. Instead, the closure of the integration of (2.14) for h is maintained by the imposition of (2.8*a,b*), which govern the evolution of the newly formed contact line (cf. Pegler *et al.* 2013*b*).

Condition (3.1) presupposes that the flow is introduced horizontally at the source. While horizontal flow need not necessarily apply at a given source distribution, where vertical flows can be driven locally by an effective point injection or within a region of buoyancy-driven upwelling, horizontal flow can nevertheless be expected to arise a short distance from it. By conducting a scaling analysis (see appendix A), the transition is found to be characterized by the length scale $\mathscr{D} \equiv q_0/\phi U$, which measures the distance on which the vertical buoyancy gradient becomes comparable to any vertical pressure gradients specified at the injection (Pegler *et al.* 2013*b*).

Forming scalings between the terms in the complete set of equations (2.7), (2.8), (2.14) and (3.2*a*), we can construct the intrinsic scales of horizontal length, time and velocity

$$\mathscr{L} \equiv \frac{UH^2}{q_0}, \quad \mathscr{T} \equiv \frac{\phi UH^3}{q_0^2}, \quad \mathscr{U} \equiv \frac{q_0}{H}, \tag{3.3a,b,c}$$

respectively. The scale (3.3*c*) represents the Darcy velocity of the source flux distributed across the depth and width of the aquifer. The scale (3.3*b*) characterizes the time taken for a two-dimensional gravity current supplied at a constant flux into an unconfined porous medium to attain the depth of the aquifer H. The length scale (3.3*a*) characterizes the horizontal distance propagated by the current in that time.

We use (3.3*a,b,c*) to non-dimensionalize the system according to

$$x \equiv \mathscr{L}\hat{x}, \quad t \equiv \mathscr{T}\hat{t}, \quad h \equiv H\hat{h}, \quad u = \mathscr{U}\hat{u}. \tag{3.4}$$

With hats dropped, the dimensionless forms of the two contributions to the velocity of the injected current in (2.10) become

$$u^p = \frac{1}{h + M(1-h)}, \quad u^g = \frac{-M(1-h)}{h + M(1-h)}\frac{\partial h}{\partial x}, \tag{3.5a,b}$$

respectively. The governing equation (2.14) becomes

$$\frac{\partial h}{\partial t} + \frac{\partial}{\partial x}[h(u^p + u^g)] = \frac{\partial h}{\partial t} + \frac{\partial}{\partial x}\left[\frac{h\left\{1 - M(1-h)\dfrac{\partial h}{\partial x}\right\}}{h + M(1-h)}\right] = 0. \tag{3.6}$$

The condition on the slope of the interface (3.2*a*), applicable before the current makes contact with the lower boundary ($h < 1$), becomes

$$-h\frac{\partial h}{\partial x} = 1 \quad (x = 0), \tag{3.7}$$

and conditions (2.7*a,b*) and (2.8*a,b*) become

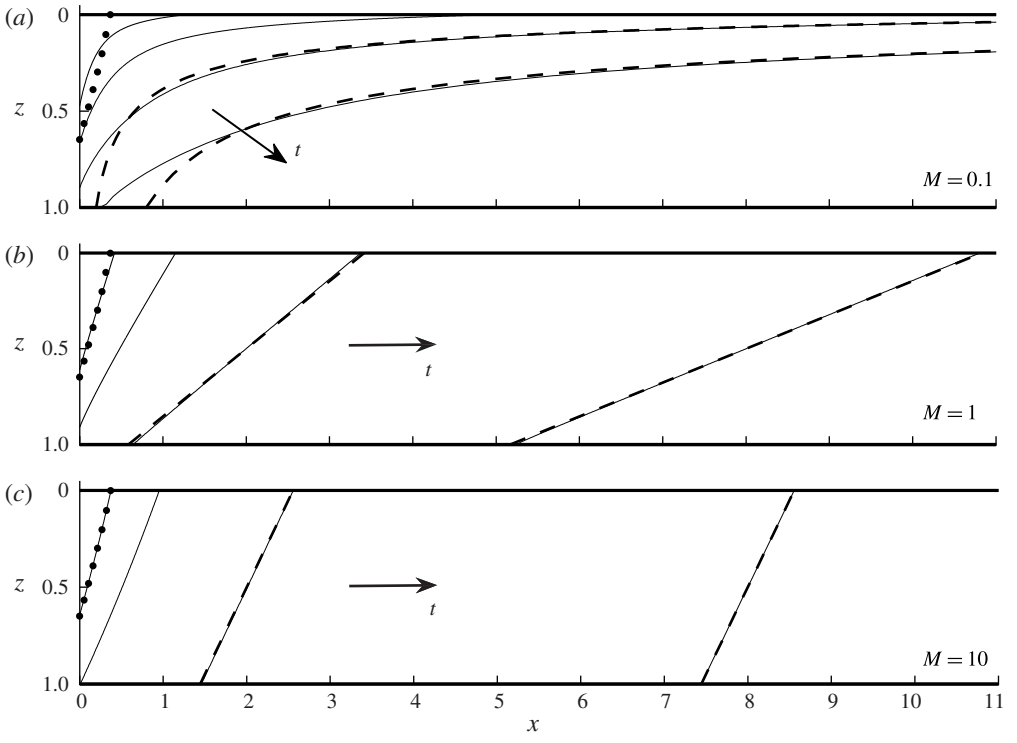

FIGURE 3. The evolution of the interface $h(x, t)$ for mobility ratios of (a) $M = 0.1$, (b) $M = 1$ and (c) $M = 10$, shown at times $t = 0.125,\ 0.5,\ 2$ and 8, illustrating the transition from the early-time buoyancy-driven similarity solution (3.10), shown as a dotted curve at $t = 0.125$, towards the late-time asymptotes (3.19), (3.32) and (3.37*b*) that apply respectively when $M < 1$, $M = 1$ and $M > 1$, each shown as dashed curves at $t = 2$ and 8.

$$h = 0, \quad \dot{X}_U = u = M^{-1} - \frac{\partial h}{\partial x} \quad (x = X_U), \tag{3.8a,b}$$

$$h = 1, \quad \dot{X}_L = u_a = M + M\frac{\partial h}{\partial x} \quad (x = X_L), \tag{3.9a,b}$$

where (3.9*a*,*b*) are imposed only after the current contacts the lower boundary ($h = 1$). The dimensionless model system above depends only on the mobility ratio M.

Three illustrative numerical solutions to (3.6)–(3.9) in the cases of $M = 0.1,\ 1$ and 10 are shown at times $t = 0.125,\ 0.5,\ 2$ and 8 as solid curves in figure 3(*a*–*c*). These solutions were calculated using a partially implicit finite-difference scheme of second order initialized using the early-time asymptotic solution described in § 3.1 below. The evolution of the two contact lines $X_U(t)$ and $X_L(t)$, and that of the horizontal distance between them $\Delta X(t) \equiv X_U - X_L$, are plotted as solid curves in figure 4(*a*,*b*), respectively. In all three cases of M, the flow evolves from an early-time regime in which the current lies in contact only with the upper boundary and has a frontal contact line X_U that evolves in proportion to $t^{2/3}$ (cf. Huppert & Woods 1995). At a certain time, the current makes contact with the lower surface ($h(0, t) = 1$), forming the second contact line X_L, which advances abruptly from $x = 0$ with a finite velocity.

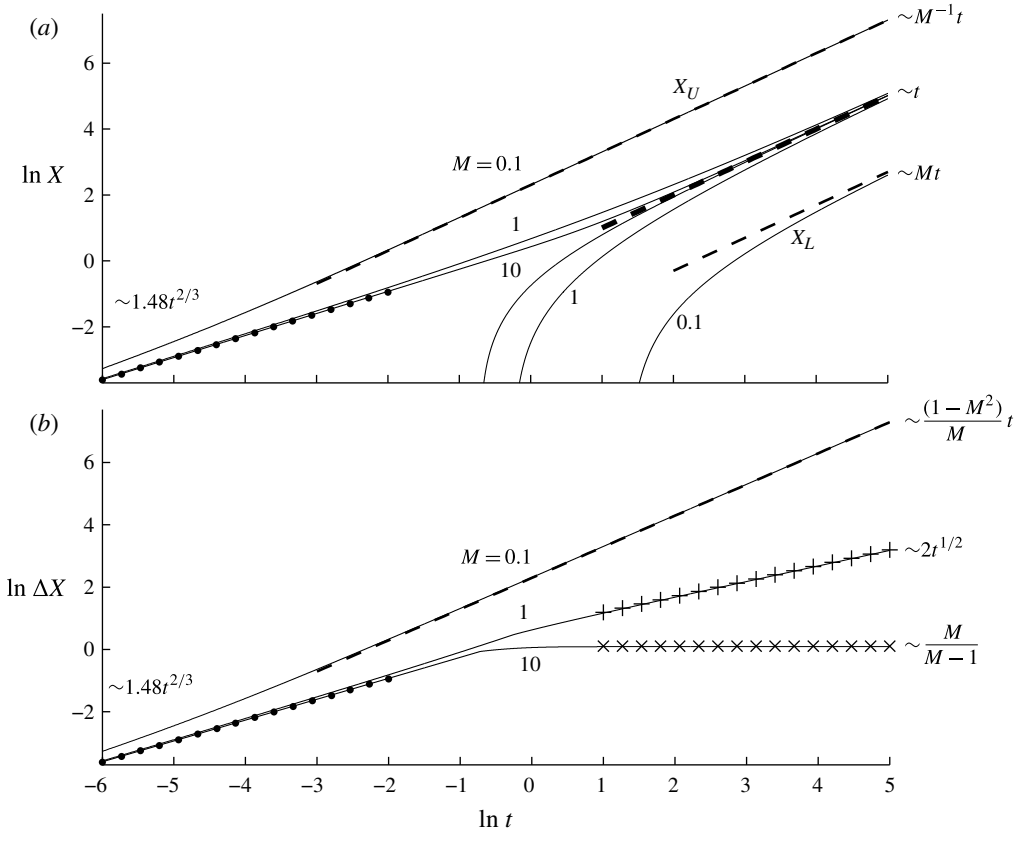

FIGURE 4. The evolution of (*a*) the upper and lower contact lines, $X_U(t)$ and $X_L(t)$, and (*b*) the horizontal distance between them, $\Delta X(t) \equiv X_U - X_L$, for the three mobility ratios $M = 0.1$, 1 and 10 (all solid lines). The early-time asymptote (3.10*b*), applicable for all values of M, is shown as a dotted line. In panel (*a*), the late-time asymptotic positions of the two contact lines (3.20*a,b*) applicable for $M < 1$ are shown as the thin dashed lines in the case $M = 0.1$; the mutual asymptotic position of the contact lines (3.25) applicable for all $M \geqslant 1$ is shown as the thick dashed line. In panel (*b*), the three respective asymptotic behaviours of the length of the interface $\Delta X(t) \equiv X_U - X_L$ applicable when $M < 1$, $M = 1$ and $M > 1$, namely (3.20*c*) (dashed), (3.33*c*) (plus signs) and (3.38*c*) (crosses), are plotted.

While the interface h in the cases of $M = 1$ and 10 remains approximately linear to later times, the case $M = 0.1$ instead evolves towards a concave shape exhibiting significant spatial structure. In all cases of M, the two contact lines X_U and X_L eventually transition towards linear growth in time. If $M \geqslant 1$ then these asymptotic approaches both have the unitary prefactor ($X_U \sim X_L \sim t$) shown by the thick dashed line in figure 4(*a*). If $M < 1$, then the prefactors are different, with the distance between the contact lines growing linearly in time ($\Delta X \propto t$). The transition in power laws illustrated in figure 4 indicates the existence of separate early- and late-time regimes. We analyse these regimes, beginning with the early-time asymptotic flow in § 3.1 and subsequently the approach towards one of three possible late-time regimes in §§ 3.2–3.4.

3.1. *Early evolution*

At early times, the current is much thinner than the depth of the medium ($h \to 0$ as $t \to 0$). The quantity (2.16) measuring the relative magnitude of buoyancy gradients is then very large ($\widetilde{G} \to \infty$), indicating that the early-time flow is driven by gravity alone. With the background pressure gradient neglected ($u^p \ll u^g$), the system of equations (3.6)–(3.9) simplify to those governing a gravity current in an unconfined aquifer, where there is a single mode of evolution described by the similarity solution

$$h \sim t^{1/3} f(x/x_N), \quad X_U \sim X_U^g \equiv 1.48\, t^{2/3} \quad (t \ll M^3), \tag{3.10a,b}$$

where f is an approximately linear function that can be calculated from the numerical solution of an ordinary differential equation (Huppert & Woods 1995). The flow regime of (3.10) is governed by a balance between hydrostatic pressure gradients and those of the viscous stresses associated with the flow of the injected current. It neglects the viscous forces associated with the motion of the ambient fluid and is therefore independent of its viscosity and hence the mobility ratio M. The early-time asymptotic condition $t \ll M^3$ specifies when the regime of (3.10) applies and can be determined by finding when (3.10*a*) predicts its self-consistency, namely, when the quantity (2.16) is large ($\widetilde{G} = Mt^{-1/3} \gg 1$). The profile of (3.10*a*) is plotted as a dotted curve in figure 3(*a–c*), where it is seen to agree well with the early-time numerical solution at $t = 0.125$ for the examples with $M = 1$ and 10. There is weaker agreement when $M = 0.1$ in accordance with the asymptotic condition $t \ll M^3 = 0.001$ becoming sufficiently restrictive that it is not satisfied when $t = 0.125$. Thus, while the asymptote of (3.10) is itself independent of M, the time scale on which the flow transitions away from it is strongly dependent on M.

In order to view the variations between these time scales more clearly, we calculate the transition time t_g defined as the time at which the frontal position first extends to beyond 10 % of the value predicted by (3.10*b*), or

$$X_U^g(t_g) = 0.9 X_U(t_g). \tag{3.11}$$

The time t_g, plotted against M in figure 5, increases with M, which is consistent with the cubic dependence on M contained in the asymptotic condition of (3.10). This trend occurs because the viscous drag associated with displacing the ambient fluid becomes a more significant dynamical constraint as it becomes more viscous relative to the injected fluid. In the idealized case of inviscid injected fluid ($M \to 0$), for example, the only resistance to motion is associated with that of the ambient fluid, and the balance underlying (3.10) never applies. In the opposite limit of inviscid ambient fluid ($M \to \infty$), there is no resistance to ambient fluid motion, so gravity-driven spreading (3.10) dominates the dynamics of the current, at least up to the time when it contacts the lower boundary.

The regime of buoyancy-driven flow described by (3.10), while a self-consistent asymptote at early times, cannot remain so at later times because (3.10*a*) predicts that the current will eventually thicken to intersect the lower boundary. The breakdown of (3.10) is also reflected by its prediction that $\widetilde{G} \sim t^{-1/3} \to 0$ as $t \to \infty$ and hence that the contribution to the velocity due to the background pressure gradients u_p necessarily intervenes at intermediate time scales. As these gradients become more influential, the flow transitions towards one of three different late-time regimes of flow depending on whether the mobility ratio is less than ($M < 1$), equal to ($M = 1$) or larger than ($M > 1$) unity.

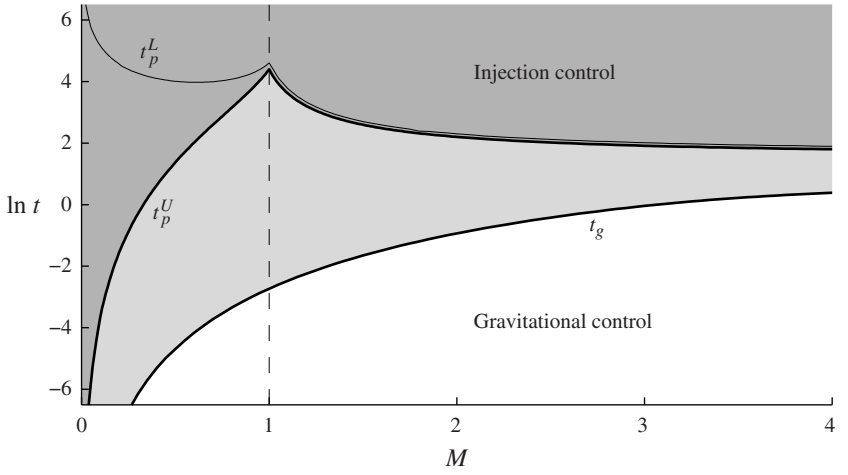

FIGURE 5. The characteristic times t_g on which the frontal position of the current transitions away from the early-time gravity-driven similarity solution, defined by (3.11), plotted against the mobility ratio M. The times t_p^U and t_p^L on which the upper and lower contact lines transition to their respective late-time asymptotes, defined by (3.21*a,b*) for $M < 1$ and by (3.39*a,b*) for $M \geqslant 1$, are shown as a thick and thin curve, respectively. The regimes in which the frontal position is controlled by gravity or by the injection pressure are shown by the white and the darker shaded regions, respectively. The intermediate region between them, in which both controls are comparable, is shown by the lighter shading. The transition times t_U^p and t_L^p are effectively equal for $M \geqslant 1$ but differ significantly for $M < 1$.

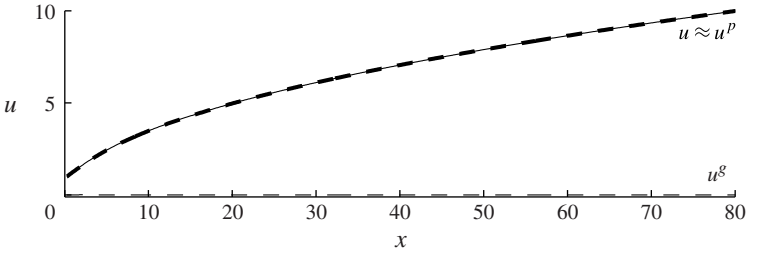

FIGURE 6. The late-time spatial distribution of the velocity $u \equiv u^p + u^g$ of the upper fluid (3.5) for $M = 0.1$, obtained from our numerical solution and shown at the representative late time of $t = 8$. The individual contributions to the velocity u (solid) due the gradient in background pressure u^p (thick dashed) and gravitational hydrostatic pressure u^g (thin dashed), defined by (3.5*a,b*), are plotted, illustrating the emergence of background-pressure-dominated flow $u \approx u^p$ (3.12). The lower contact line is yet to form at this relatively late time, which reflects the endurance of gravity-driven flow near the source (see the discussion surrounding (3.21)).

3.2. *More viscous ambient fluid*

To reveal the late-time dynamics that arise in cases where the injected fluid is less viscous than the ambient fluid ($M < 1$), we have plotted the two contributions to the velocity of the upper fluid layer u^p and u^g for the illustrative case of $M = 0.1$ in figure 6 at the characteristic late time of $t = 8$. A comparison between them shows

that the gravitational contribution u^g is negligible, with the flow becoming dominated by the influence of the background pressure gradient,

$$u^p \gg u^g \quad (t \gg 1). \tag{3.12}$$

The decay of the gravitational contribution to the flow is consistent with the reduction in the gradient of the interface $\partial h/\partial x \to 0$ with time illustrated by our numerical solution in figure 3(*a*). This reduction causes the gradient-dependent contribution of u^g (3.5*b*) to decay with time while the gradient-independent contribution of u^p (3.5*a*) remains significant. As we noted in § 3.1, the reduction in gradient is predicted to occur as the flow transitions to times of order unity by the early-time similarity solution (3.10). As we detail below, this reduction in gradient is also driven, and thus self-consistently maintained, by the emerging dynamics in which the background pressure becomes significant. To show this, we presuppose that (3.12) applies and confirm its self-consistency as a late-time asymptotic relationship for $M < 1$, *a posteriori*.

With u^g neglected in (3.6), (3.8) and (3.9), these equations simplify to

$$\frac{\partial h}{\partial t} = -\frac{\partial}{\partial x}[hu^p] = -\frac{\partial}{\partial x}\left[\frac{h}{h + M(1-h)}\right], \tag{3.13}$$

$$h = 0, \qquad \dot{X}_U = u^p = M^{-1} \quad (x = X_U), \tag{3.14a,b}$$

$$h = 1, \qquad \dot{X}_L = u^p_a = M \qquad (x = X_L). \tag{3.15a,b}$$

Equations (3.13)–(3.15) have been derived previously in the context of flows dominated by background flow in petroleum engineering (Dake 2010). Equation (3.13) is a first-order nonlinear advection equation. The velocities of the contact lines (3.14*a,b*) are simply constant, taking the limiting values of u^p and u^p_a attained where the interface contacts the upper or lower boundary, the former illustrated earlier in figure 2.

We briefly review the calculation of a similarity solution to (3.13)–(3.15) by Gunn & Woods (2011) and subsequently present new results relating to its dynamical stability and role as a late-time asymptote when buoyancy gradients are present. Note that there is no horizontal length scale in the reduced system (3.13)–(3.15), which indicates that it supports a similarity solution. Recasting (3.13)–(3.15) in terms of the similarity coordinate $\eta \equiv t^{-1}x$, we obtain

$$t\frac{\partial h}{\partial t} - \eta\frac{\partial h}{\partial \eta} = -\frac{\partial}{\partial \eta}\left[\frac{h}{h + M(1-h)}\right], \tag{3.16}$$

$$h = 0, \qquad t\dot{\eta}_U + \eta_U = M^{-1} \quad (\eta = \eta_U), \tag{3.17a,b}$$

$$h = 1, \qquad t\dot{\eta}_L + \eta_L = M \qquad (\eta = \eta_L), \tag{3.18a,b}$$

where $\eta_U \equiv t^{-1}X_U$ and $\eta_L \equiv t^{-1}X_L$. Unlike Gunn & Woods (2011), we have retained the terms containing derivatives of time t for the purpose of conducting a stability analysis. Equations (3.16)–(3.18) are satisfied by the closed-form similarity solution

$$h = h^p(\eta) \equiv \frac{-M + (M/\eta)^{1/2}}{1 - M}, \tag{3.19}$$

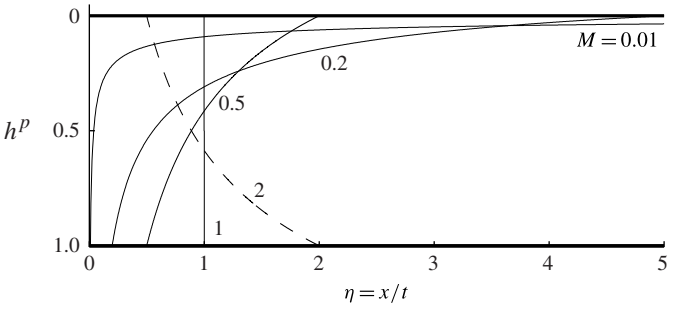

FIGURE 7. The similarity solution (3.19) that describes the interface position h when the flow is driven purely by the background pressure ($u = u_p$), shown for a selection of mobility ratios $M = 0.01,\ \ 0.2,\ \ 0.5$ and 1. The hypothetical case $M = 2$, shown by the dashed curve, violates the vertical ordering of the layers required for a stable interface under gravity, reflecting the inconsistency of (3.12) as a late-time balance for $M > 1$.

which we have plotted for a range of mobility ratios M in figure 7 and compared against our numerical data in the case of $M = 0.1$ in figure 3(a) at $t = 2$ and 8 (both dashed). The shape of (3.19) becomes increasingly concave as M is reduced, eventually exhibiting a near-horizontal profile at the upper contact line and a near-vertical profile at the lower contact line. The concave shape is caused by the nonlinear relationship between the depth of the current h and the background-pressure-driven velocity $u = u^p$ when $M < 1$, illustrated earlier in figure 2. The preference for the less viscous injected fluid to flow faster as its thickness decreases and forming a relatively thin layer to minimize viscous dissipation is analogous to the instability mechanism underlying Saffman–Taylor fingering (Saffman & Taylor 1958). In the opposing limit of $M \to 1$, (3.19) approaches the vertical interface, which is consistent with the equivalence of the background-pressure-driven velocities of the two layers $u^p \equiv u_a^p$ in that limit (see § 3.3 below). Note that, when re-expressed in terms of dimensional variables, the prediction of (3.19) is independent of the permeability k, which reflects the fact that its shape is entirely a consequence of the relative flow rates due to the differing viscosities between the layers.

The asymptotic positions of the contact lines X_L and X_U, along with the horizontal distance between them $\Delta X \equiv X_U - X_L$, are predicted by (3.17$b$) and (3.18$b$) to evolve linearly in time according to

$$X_U \sim M^{-1}t, \quad X_L \sim Mt, \quad \Delta X \sim \frac{1 - M^2}{M}t \quad (t \to \infty). \tag{3.20a,b,c}$$

The late-time asymptotes (3.20a,b,c) are confirmed by our numerical data for $M = 0.1$ shown in figure 4(a,b). While the upper contact line X_U becomes well described by (3.20a) in relatively short time ($t \lesssim 0.01$), the lower contact line instead takes very much longer to approach (3.20b) ($t \gtrsim 100$). To visualize these variations in greater detail, we compute the two times t_U^p and t_L^p defined by

$$X_U(t_U^p) = 0.9[Mt_U^p], \quad X_L(t_L^p) = 0.9[M^{-1}t_L^p] \quad (M \leqslant 1), \tag{3.21a,b}$$

which characterize the times on which the two contact lines are within 10 % of their respective asymptotes (3.20a,b). These times are shown by the thin and thick curves in figure 5 for $M < 1$ (appropriate extensions of (3.21a,b) to $M \geqslant 1$ are considered later

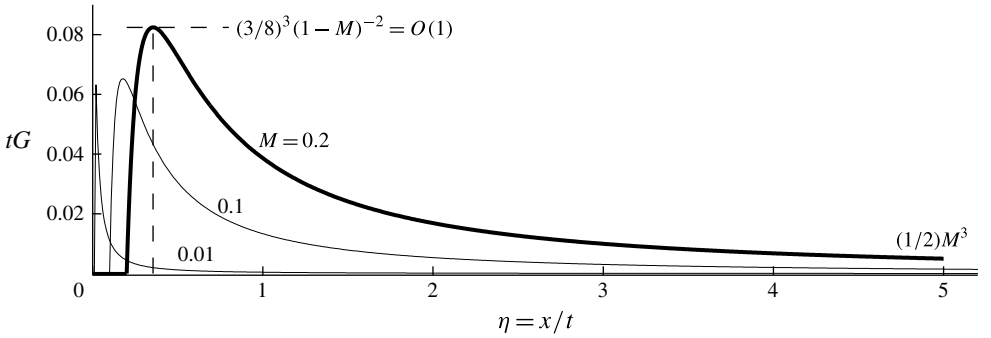

FIGURE 8. The ratio G of the buoyancy-driven velocity and the injection-driven velocity, defined by (2.15), scaled with time t, evaluated across the extent of the late-time similarity solution (3.19) for a selection of mobility ratios given by $M = 0.2$ (thick), $M = 0.1$ and 0.01 (both thin). The plot illustrates the variation in tG from a maximum value of $O(1)$ near the lower contact line ($\eta = M$) to the much smaller value of $O(M^3)$ at the upper contact line ($\eta = M^{-1}$), occurring as a consequence of the significant difference in gradient between these two points (see figure 7). The contrast between values of G along the length of the flow explains why the contribution to spreading due to gravity remains more significant near the source relative to its contribution downstream.

in § 3.4). The frontal transition time t_U^p increases with M, indicating that the front of the current becomes controlled by the background pressure gradient in a shorter time when the ambient fluid is more viscous. This trend reflects the fact that, with more viscous ambient fluid, the relationship between u_p and h given by the first term in (2.10) implies that the background pressure gradient stretches the interface faster and hence causes the buoyancy gradients u_g to decay more rapidly. The transition time t_U^p is maximized when M is close to unity because the viscosity contrasts that cause the stretching of the interface by the background pressure are uniquely absent when $M = 1$, thus allowing the contribution to the flow due to the gradients in buoyancy u_g to remain significant to longer times.

While the transition time of the upper contact line t_U^p increases with M, that of the lower contact line t_L^p exhibits the opposite trend, with t_L^p increasing to infinity as M reduces to zero. This is surprising because t_U^p and t_L^p both measure times on which the flow transitions towards the same asymptotic state (3.19). The significant contrast between them for $M \to 0$ is caused by the different times on which buoyancy gradients remain significant between the front of the current and the region near the source. More specifically, these differences are caused by the dramatic variations in slope $\partial h/\partial x$ along the interface predicted by (3.19), illustrated in the case of $M = 0.01$ in figure 7, for example. The significance of buoyancy-driven flow across the layer can be measured by the quantity G defined earlier by (2.15), which we have plotted against η for the asymptotic state (3.19) in figure 8. The value of G decays from a maximum of $G(16M/9, t) = O(t^{-1})$ near the lower contact line towards the much smaller value of $G(M^{-1}, t) = O(M^3 t^{-1})$ at the upper contact line. These variations in G explain why buoyancy controls the flow near the lower contact line for times much longer than that near the upper contact line.

We analyse the convergence of the flow towards the similarity solution (3.19) by conducting a linear stability analysis of the base state (3.19). Substituting perturbation expansions for the interface height $h = h^p(\eta) + h_1(\eta, t)$ and positions of the contact

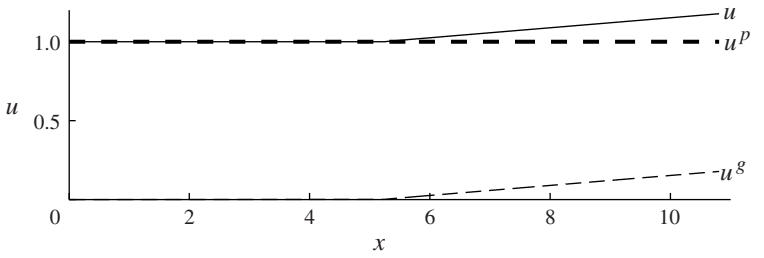

FIGURE 9. The late-time spatial distribution of the velocity $u \equiv u^p + u^g$ of the upper fluid (3.5) as a function of x for $M = 1$, obtained from our numerical solution at $t = 8$. The individual contributions to u (solid) due the gradient in background pressure u^p (thick dashed) and hydrostatic pressure u^g (thin solid), defined by (3.5*a,b*), are plotted, illustrating the constancy of u^p (3.25) and the gradual acceleration of the upper fluid layer above this value due to gravitational spreading u^g.

lines $X_U = M^{-1}t + X_{U,1}$ and $X_L = Mt + X_{L,1}$, where $h_1, X_{U,1}$ and $X_{L,1}$ are small first-order corrections, into (3.13), (3.14*a*) and (3.15*a*) and neglecting terms quadratic in small quantities, we obtain the linearized equations

$$t\frac{\partial h_1}{\partial t} + h_1 = 0, \qquad \begin{matrix} X_{U,1} = aM^{-1}h_1, \\ X_{L,1} = aMh_1, \end{matrix} \tag{3.22a,b,c}$$

where $a \equiv 2(1 - M)$. We can readily integrate (3.22*a*) to obtain

$$h_1 = t^{-1}F(\eta), \qquad \begin{matrix} X_{U,1} = -[aM^{-1}F(M^{-1})]t^{-1}, \\ X_{L,1} = -[aMF(M)]t^{-1}, \end{matrix} \tag{3.23a,b,c}$$

where $F(\eta)$ describes the shape of the correction h_1 at the dimensionless time $t = 1$ and could be determined by suitably matching (3.23) to the transient solution at times of order unity. The results (3.23*a,b,c*) show that the similarity solution (3.19) is a stable attractor and that any perturbation to (3.19) closely retains its earlier shape F but decays relatively to it as t^{-1}.

3.3. *Equally viscous fluids*

When the two fluid layers are equally viscous ($M = 1$), the contribution to their velocities due to the background pressure, given by u^p and u_a^p in (2.10) and (2.11), are both equal and given at all times by the uniform dimensionless value

$$u^p \equiv u_a^p \equiv 1, \tag{3.24}$$

which we have plotted as a thick dashed line in figure 9. Our earlier plot of the contact-line positions $X_U(t)$ and $X_L(t)$ for $M = 1$ in figure 4(*a*) indicated that they both approach the same asymptote

$$X_L \sim X_U \sim t \quad (t \to \infty), \tag{3.25}$$

which is consistent with the late-time position that is implied if the uniform flow (3.24) were to independently drive the flow. This indicates that, like the solutions for

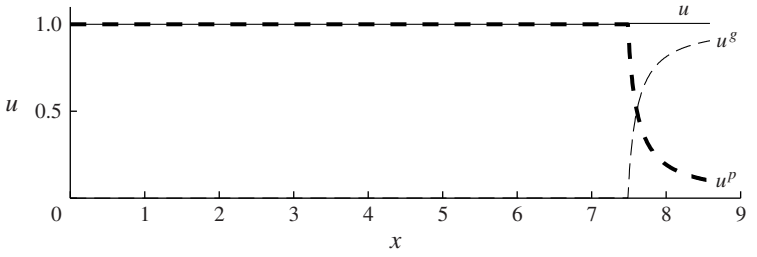

FIGURE 10. The late-time spatial distribution of the velocity $u \equiv u^p + u^g$ of the upper fluid (3.5) as a function of x for $M = 10$, obtained from our numerical solution at $t = 8$. The individual contributions to u (solid) due the gradient in background pressure u^p (thick dashed) and hydrostatic pressure u^g (thin solid), defined by (3.5*a*,*b*), are plotted. The figure illustrates the asymptotic uniformity of the velocity $u \sim 1$ and the mutual significance of the background pressure and buoyancy gradients $u^p \sim u^g$ in a region that approaches the finite length (3.38*c*) at the front of the current.

$M < 1$ described in § 3.2 above, the buoyancy gradient eventually diminishes at late times relative to the background pressure gradient ($u^g \ll u^p$).

While (3.25) implies that the positions of the contact lines become equal relative to the extent of the flow, our numerical solution presented in figure 3(*b*), shows that lateral expansion of the interface occurs at first order due to buoyancy-induced spreading u^g. This spreading is also illustrated by the growth of the interfacial extent ΔX shown in figure 4(*b*) and by the plot of u^g in figure 9, which shows that buoyancy drives the upper fluid to speeds above those induced by the background-pressure-driven flow (3.24) alone. The first-order expansion under buoyancy can be analysed more directly by recasting the system in terms of the moving coordinate $\xi \equiv x - t$ (Bear 1988; Huppert & Woods 1995), which shifts the flow into the frame of the leading-order position of the contact lines (3.25). In terms of (ξ, t) and the shifted frontal positions $\Xi_U = X_U - t$ and $\Xi_L = X_L - t$, equation (3.6) and conditions (3.8)–(3.9) become

$$\frac{\partial h}{\partial t} = -\frac{\partial [h u^g]}{\partial \xi} = \frac{\partial}{\partial \xi}\left[h(1-h)\frac{\partial h}{\partial \xi}\right], \tag{3.26}$$

$$h = 0, \quad \dot{\Xi}_U = u^g = -\frac{\partial h}{\partial \xi} \quad (\xi = \Xi_U), \tag{3.27a,b}$$

$$h = 1, \quad \dot{\Xi}_L = u^g = \frac{\partial h}{\partial \xi} \quad (\xi = \Xi_L), \tag{3.28a,b}$$

respectively. Recasting (3.26)–(3.28) in terms of the similarity coordinate $\zeta \equiv t^{-1/2}\xi$, we obtain

$$t\frac{\partial h}{\partial t} - \frac{1}{2}\zeta\frac{\partial h_1}{\partial \zeta} = \frac{\partial}{\partial \zeta}\left[h(1-h)\frac{\partial h}{\partial \zeta}\right], \tag{3.29}$$

$$h = 0, \quad t\dot{Z}_U + \frac{1}{2}\frac{\partial Z_U}{\partial \zeta} = -\frac{\partial h}{\partial \zeta} \quad (\zeta = Z_U), \tag{3.30a,b}$$

$$h = 1, \quad t\dot{Z}_L + \frac{1}{2}\frac{\partial Z_L}{\partial \zeta} = \frac{\partial h}{\partial \zeta} \quad (\zeta = Z_L), \tag{3.31a,b}$$

where $Z_U \equiv t^{-1/2}\Xi_U$ and $Z_L \equiv t^{-1/2}\Xi_L$. Equations (3.29)–(3.31) support the closed-form similarity solution (Huppert & Woods 1995)

$$h = h_0(\zeta) \equiv \tfrac{1}{2}(1-\zeta), \quad Z_U = 1, \quad Z_L = -1, \tag{3.32a,b,c}$$

representing a linear interface. This asymptote, plotted as a dashed line in figure 3(*b*) at $t = 2$ and 8, is seen to be attained rapidly by the numerical solution, with the speed of attraction probably caused by the lack of any significant morphological change between (3.32) and the nearly linear interface established during the early-time regime of (3.10). On reverting back to the frame of the laboratory, (3.32*b,c*) provide the positions of the upper and lower contact lines, along with the horizontal distance between them, as

$$X_L \sim t - t^{1/2}, \quad X_U \sim t + t^{1/2} \quad \Delta X \sim 2t^{1/2}. \tag{3.33a,b,c}$$

The asymptotic convergence of the horizontal distance ΔX towards (3.33*c*) is illustrated for $M = 1$ in figure 4(*b*), where (3.33*c*) is plotted as a line of crosses. The characteristic transition times $t_U^p \approx 81$ and $t_L^p \approx 100$, defined by (3.21), are of comparable magnitude when $M = 1$, which can be attributed to the symmetry of the linear asymptotic profile (3.32) about its centre. As noted above in § 3.2, the maximum of t_U^p at $M = 1$ amongst cases of $M \leqslant 1$ reflects the absence of any stretching of the interface by the background pressure gradient.

By conducting a perturbation analysis about the base state (3.32), we can determine (see appendix B) that any perturbation to the base state evolves at late times as

$$h \sim \tfrac{1}{2}[1 - (1 + At^{-1})\zeta] \quad (t \to \infty), \tag{3.34}$$

where A is a constant, showing that the similarity solution (3.32) is an attractor. In common with the similarity solutions considered in § 3.2, the first-order correction decays algebraically as t^{-1}. Unlike that case, however, (3.34) is independent of the earlier shape of the perturbation. This loss of information of the initial conditions is associated with the parabolic property of (3.6) or, in more physical terms, the dissipation of perturbations to the interface under the action of buoyancy. These are absent to leading order in the late-time regime described by (3.23).

3.4. *Less viscous ambient fluid*

When the ambient fluid is more viscous ($M > 1$), (2.13*a*) implies that the background pressure gradient acts to drive the lower fluid faster than the upper fluid ($u_a^p > u^p$), thus acting to steepen the interface. Without the intervention of gravity, these forces would drive the interface to overturn in a manner reminiscent of a breaking wave. This is different from the case $M < 1$ considered above in § 3.2, where the background pressure gradient instead acts to stretch the interface, causing the gradient of the interface $\partial h/\partial x$, and hence the gradient in buoyancy, to decay. In the case $M > 1$, the steepening of the current by the background pressure gradient instead allows buoyancy gradients to remain significant along the interface and, as can be inferred from our numerical solution in figure 3(*c*), counteract the progressive steepening of the interface that would be caused in the absence of gravity. The inconsistency of uniformly neglecting spreading due to buoyancy (3.12) at late times when $M < 1$ is also reflected by the fact that the associated hypothetical prediction of (3.19), shown by the example of $M = 2$ in figure 7, requires the heavier fluid to lie above the lighter, an arrangement that is unattainable under the action of buoyancy-driven spreading.

Following the approach in § 3.3 above, we again recast (3.6) in terms of the shifted coordinate $\xi = x - t$ to give

$$\frac{\partial h}{\partial t} - \frac{\partial h}{\partial \xi} = -\frac{\partial}{\partial \xi}[hu]. \tag{3.35}$$

Integrating the steady form of (3.35), we obtain

$$h = hu + \text{const.} \quad \text{and hence} \quad u = \frac{1 - M(1-h)\dfrac{\partial h}{\partial \xi}}{h + M(1-h)} = 1 \tag{3.36a,b}$$

on imposition of the conditions $h = u = 1$ at $x = X_L$. Rearrangement of (3.36*b*) yields

$$\frac{\partial h}{\partial \xi} = -\frac{M-1}{M} \quad \text{and hence} \quad h = h_0(\xi) \equiv \frac{1}{2} - \frac{M-1}{M}\xi \tag{3.37a,b}$$

on integration subject to the condition of symmetry, $h(0) = 1/2$. By imposing conditions (3.8*a*) and (3.9*a*) on (3.37*b*), we obtain the positions of the contact lines, along with the horizontal distance between them, as

$$X_U \sim t + \frac{l}{2}, \quad X_L \sim t - \frac{l}{2}, \quad \Delta X \sim l \equiv \frac{M}{M-1}, \tag{3.38a,b,c}$$

respectively. The asymptotic interface profile (3.37*b*) closely matches our numerical data in figure 3(*c*), where it is plotted as a dashed line at $t = 2$ and 8 for $M = 10$. The constant slope of the linear asymptote (3.37*a*) represents the threshold at which buoyancy-driven spreading balances the overturning effect of the background pressure gradient. In contrast to the late-time regimes of $M \leqslant 1$, for which the interface expands indefinitely, the regime of $M > 1$ is characterized by the convergence of the extent of the interface towards a constant length (3.38*c*) illustrated by the line of crosses in figure 4(*b*). The length (3.38*c*) decreases with M, reflecting the fact that the interface must steepen more for the buoyancy-driven flow to balance the larger viscous forces associated with the motion of the ambient fluid. There is a distinguished minimum asymptotic length $\Delta X \sim 1$ occurring in the limit of inviscid ambient fluid $M \to \infty$.

The continuation of the characteristic times of transition (3.21*a,b*) for $M > 1$ can be defined with respect to the leading-order positions of the contact lines (3.38) by

$$X_U(t_U^p) = 0.9 t_U^p, \quad X_L(t_L^p) = 0.9 t_L^p \quad (M \geqslant 1), \tag{3.39a,b}$$

which we have plotted for $M > 1$ in figure 5. Like the case $M = 1$, the transition times t_U^p and t_L^p are effectively equal for $M \geqslant 1$ because the linear asymptotic state (3.37*b*) is similarly symmetrical about its centre. The trend of increasing t_L^p reverses sharply once $M > 1$ because, while the background pressure drives the interface to stretch for $M < 1$, it has the opposite effect for $M > 1$, causing the interface to compress laterally relative to the extent of the current and driving the interface to steepen in shorter time.

By conducting a linear stability analysis of the base state (3.37*b*), we can determine (see appendix C) that the first-order correction evolves according to

$$h \sim h_0 + A\,\mathrm{e}^{-\Lambda t} F_M(\xi) \quad (t \to \infty), \tag{3.40}$$

where $\Lambda = \Lambda(M)$ is the exponent of decay, A is a matching constant and the function $F_M(\xi)$ describes the late-time shape of the correction for a given value of $M > 1$.

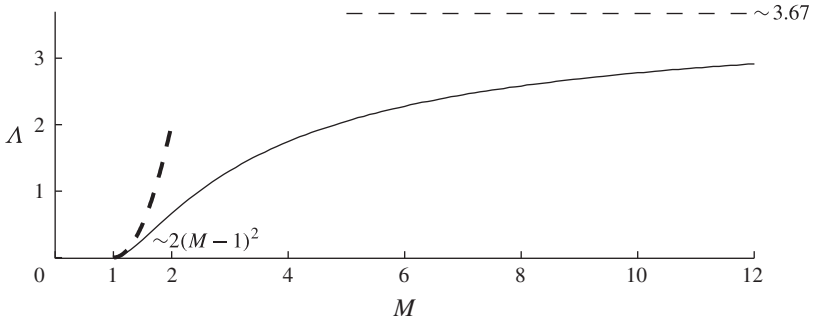

FIGURE 11. The exponent of decay $\Lambda(M)$ in the time-dependent factor $\mathrm{e}^{-\Lambda t}$ describing the asymptotic decay of perturbations to the position of the interface (3.40) when $M > 1$ plotted against the mobility ratio M. The asymptotes $\Lambda \sim 2(M-1)^2$ (thick solid) and $\Lambda \sim 3.67$ (dashed) that apply in the limits of equally viscous fluids ($M \to 1^+$) and of inviscid ambient fluid ($M \to \infty$) (see appendix C) are shown by the thick and thin dashed curves, respectively.

As illustrated in figure 11, the exponent of decay Λ is positive for all values of $M > 1$, confirming that (3.37*b*) is an attractor. Its increase with M is consistent with the corresponding decreases of both t_U^p and t_L^p with $M > 1$ shown earlier in figure 5. In the limit of inviscid ambient fluid ($M \to \infty$), the exponent is given by the asymptotic value $\Lambda \sim 3.67$ shown by the thin dashed line in figure 11. The exponential decay of the perturbation described by (3.40) contrasts with the algebraic decay determined in §§ 3.2 and 3.3 above in cases of $M \leqslant 1$, reflecting a general principle that perturbations to similarity solutions evolve algebraically, while perturbations to steady states evolve exponentially (cf. Pegler, Lister & Worster 2012). Like the first-order correction described by (3.34) that applies in the case $M = 1$, the correction approaches an asymptotic shape $F_M(\xi)$ that is independent of any initial conditions, again attributable to the dissipation of information by gradients in buoyancy.

4. Laboratory study

We have conducted a series of laboratory experiments with which to compare our theoretical predictions. Our experiments took place in a cell formed of two Perspex sheets separated by plastic spacers (see figure 12). The gaps between the sheets and spacers were sealed using Teflon grease and the cell pressed together with clamps along its outside. The spacers formed the boundaries of a partially enclosed region of width 0.6 cm, depth 10 cm and length 200 cm, which was confined by the spacers except for a gap of length 10 cm along the upper boundary on the right-hand side of the cell. The enclosed region was filled with glass ballotini beads of diameter 2 mm, forming a porous layer. The mean porosity of the medium, $\phi \approx 0.38 \pm 0.01$, was determined by measuring the total mass of ballotini used to fill the region. This is consistent with that reported by Acton, Huppert & Worster (2001). We take the corresponding mean permeability $k \approx (3.1 \pm 0.2) \times 10^{-5}$ cm^2 measured by Acton *et al.* (2001) and used also by Golding & Huppert (2010).

We ran four sets of experiments, denoted by (a)–(d) in table 1. In sets (a) and (b), we injected fresh water, dyed by blue food colouring, into aqueous solutions of sodium chloride (brine) of two different concentrations. The brine solutions were more

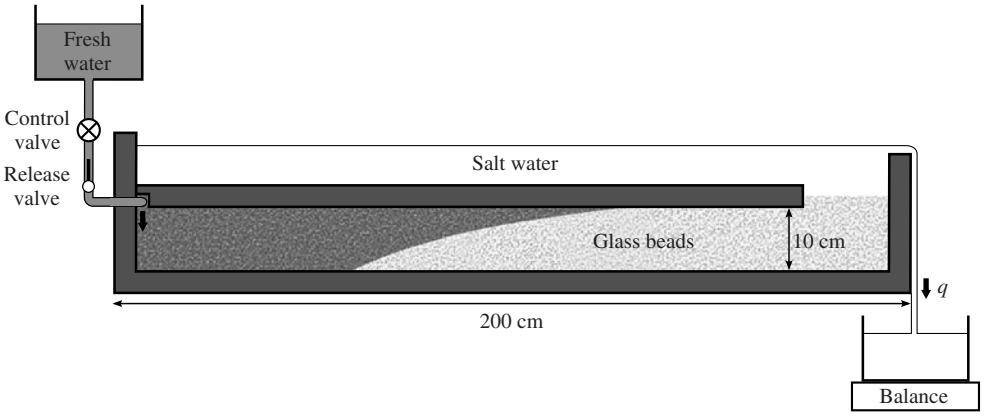

FIGURE 12. Schematic of our experimental system.

viscous than the fresh water, providing mobility ratios of $M = 0.56$ and 0.84, both less than unity. In set (c), we reversed the fluids, injecting a solution of brine into fresh water, thus yielding a case of $M = 1.83$, greater than unity. In set (d), we injected an aqueous solution of golden syrup (an approximately 40 wt% concentration) into fresh water, yielding the larger mobility ratio of $M = 5.93$. In sets (c) and (d), the injected fluids were denser than the ambient fluid, which, while opposite to the arrangement assumed in our theoretical development, can be straightforwardly accommodated by a reversal of the vertical coordinate z. The densities ρ and ρ_a and viscosities μ and μ_a of the injected and ambient fluids were measured before each experiment using a hydrometer and a U-tube viscometer to estimated tolerances of 0.001 g cm^{-3} and 0.1 cP.

The experiment was primed by filling the cell with the ambient fluid. The injection was performed using a gravity feed formed of a reservoir connected in series to a control valve, a release valve and lastly to the cell at the upper left-hand corner of the enclosed region for sets (a) and (d) and at the lower left-hand corner for sets (c) and (d). Once initiated, the injected fluid displaced the ambient fluid, causing it to spill over the right-hand edge of the cell and collect in a container, whose mass we recorded over the course of the experiment. This provided a measurement of the volumetric flux per unit width q_0 to an estimated accuracy of 0.01 cm^2 s^{-1}. The experiment was photographed at regular intervals using a camera directed towards the front of the cell, and the photographs were analysed afterwards to obtain the positions of the contact lines. The two sets of photographs shown in figure 13(*a*,*b*) illustrate the evolution of two experiments representative of sets (a) and (d), corresponding to those labelled by ☆ in table 1.

Our experiments spanned injection fluxes per unit width q_0 from 0.067 to 1.94 cm^2 s^{-1}, injected fluid viscosities μ from 0.94 to 5.52 cP, ambient fluid viscosities from 0.93 to 1.68 cP, and density differences $\Delta\rho$ from 0.079 to 0.187 g cm^{-3} (see table 1). The experimental data for the positions of the contact lines, obtained by manually measuring the length of the injected flow along the upper and lower boundaries from our photographs, are plotted in figure 14, where our theoretical predictions are shown as solid curves. Our predictions for the profile of the interface $h(x, t)$ are shown as dashed curves overlaying the time-lapse progressions in figure 13. Generally good agreement is observed between the experimental data and the predictions.

	Symbol	$M \equiv \mu/\mu_a$	q_0 (cm^2 s^{-1})	μ (cP)	μ_a (cP)	$\Delta\rho$ (g cm^{-3})
(a)	×	0.56	1.94	0.94	1.68	0.181
	◯	0.56	1.40	0.94	1.68	0.181
	☆	0.56	1.18	0.94	1.68	0.181
	△	0.56	1.10	0.94	1.68	0.181
	+	0.56	0.72	0.94	1.68	0.181
	•	0.56	0.085	0.94	1.68	0.181
(b)	×	0.84	1.61	0.97	1.15	0.079
	◯	0.84	0.42	0.97	1.15	0.079
	☆	0.84	0.15	0.97	1.15	0.079
	•	0.84	0.089	0.97	1.15	0.079
(c)	×	1.83	1.78	1.74	0.95	0.181
	◯	1.83	1.20	1.74	0.95	0.181
	•	1.83	0.25	1.74	0.95	0.181
(d)	×	5.93	0.28	5.52	0.93	0.187
	◯	5.93	0.26	5.52	0.93	0.187
	☆	5.93	0.15	5.52	0.93	0.187
	△	5.93	0.13	5.52	0.93	0.187
	•	5.93	0.067	5.52	0.93	0.187

TABLE 1. Parameter values used in our experiments.

The interface between the injected and ambient fluids remained relatively sharp across the course of each experiment, except for the nose of the currents, where the concentration of dye faded smoothly into the ambient fluid. This fading, which occurred for example in the experiment shown in figure 13(*a*), was caused by the dispersion that acts to mix adjacent fluids flowing in porous media. In cases where the injected fluid was less viscous than the ambient fluid ($M < 1$), dispersion may have been enhanced by viscous fingering at the pore scale (Taylor 1953). Dispersion was also reported to occur in the experimental studies of Lyle *et al.* (2005) and Golding & Huppert (2010). Note that the large-scale viscous fingering of the interface that would occur in the absence of gravity (Saffman & Taylor 1958) does not occur, confirming that vertical gradients in hydrostatic pressure act to stabilize the interface against the pressure gradients that would otherwise drive such an instability.

Upstream, the majority of the injected fluid only displaced pre-existing injected fluid, so dispersion was less significant in that region compared to the front of the current. Mixed fluid gradually accumulated over time as the current continued to propagate, which caused the smeared region of the flow to grow in time, as is evident in the progressions shown in figure 13. The greater significance of the smearing in causing discrepancies between the data and the predictions for $X_U(t)$ in set (a), compared to the other experiments, can be attributed to the fact that the theoretical prediction in cases of small M requires the flow to occupy a relatively thin region along the top boundary, terminating at a sharp nose. For these cases, the loss of a sharp contrast at the nose has a greater impact on the apparent extent of the current than in those cases where the predicted slope of the interface is steeper. These differences are consistent with the more significant discrepancies observed between experimental sets (a) and (d).

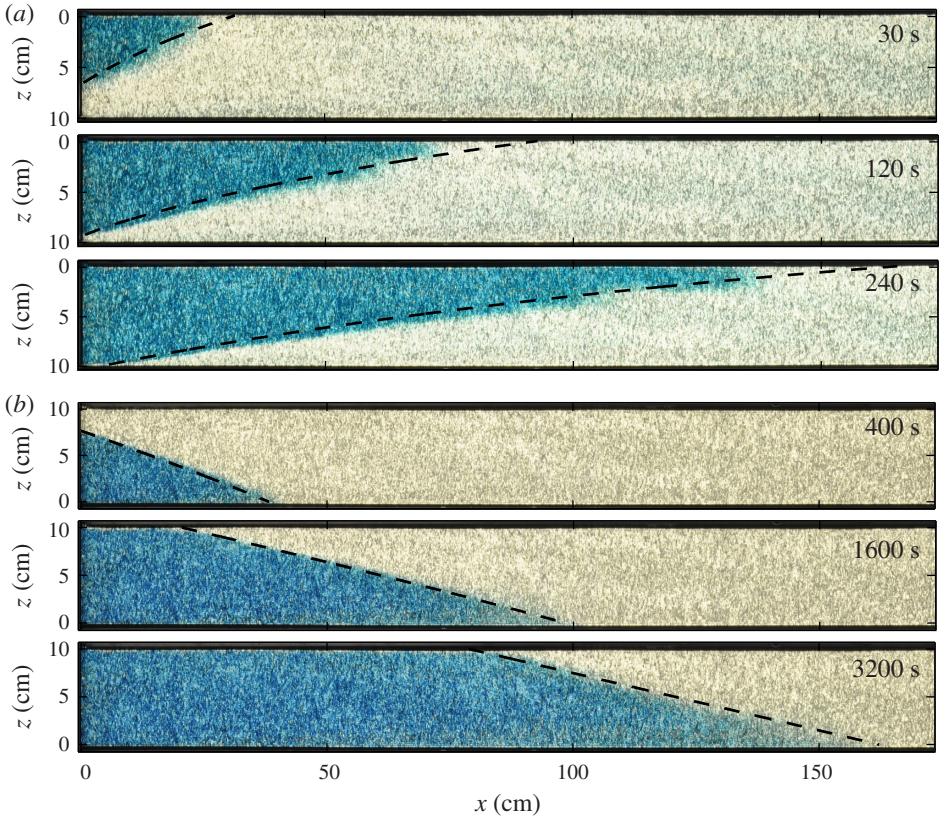

FIGURE 13. (Colour online) Images showing the evolution of the experiments labelled by the ☆ symbol from sets (a) and (d) in table 1. The theoretical predictions for the position of the interface h are shown as dashed curves in each case. In panels (a), the injected fluid (dyed fresh water) is both less viscous and lighter than the ambient brine, representing cases for which the mobility ratio is less than unity, $M < 1$. In panels (*b*), the injected fluid (a dyed solution of golden syrup) is both more viscous and denser than the ambient fresh water, representing cases of $M > 1$.

5. Geophysical discussion

We use our theoretical results to compare the importance of confinement on the dynamics of CO_2 injected between the two CCS test sites of Sleipner in the North Sea and In Salah in the Algerian desert. The Sleipner test site consists of a sandstone aquifer with an approximate total thickness of 200 m partitioned into several interstitial porous layers, of characteristic thickness $H \approx 20$ m, by a series of relatively thin and impermeable mudstone boundaries (Bickle *et al.* 2007; Boait *et al.* 2012). Representative values for the porosity $\phi \approx 0.35$, permeability $k \approx 10^{-12}$ m^2, viscosity of carbon dioxide $\mu \approx 6 \times 10^{-5}$ Pa s, viscosity of brine $\mu \approx 7 \times 10^{-4}$ Pa s, density of carbon dioxide $\rho \approx 700$ kg m^{-3}, density of brine $\rho_a \approx 1000$ kg m^{-3} and mean volumetric flux of injection $Q \approx 0.04$ m^3 s^{-1} have been documented (Boait *et al.* 2012). While the volumetric rates at which fluid enters each interstitial layer need not equal Q, since not all of the CO_2 necessarily leaks through to the upper horizons, they must nevertheless be comparable to or less than Q across the nine layers.

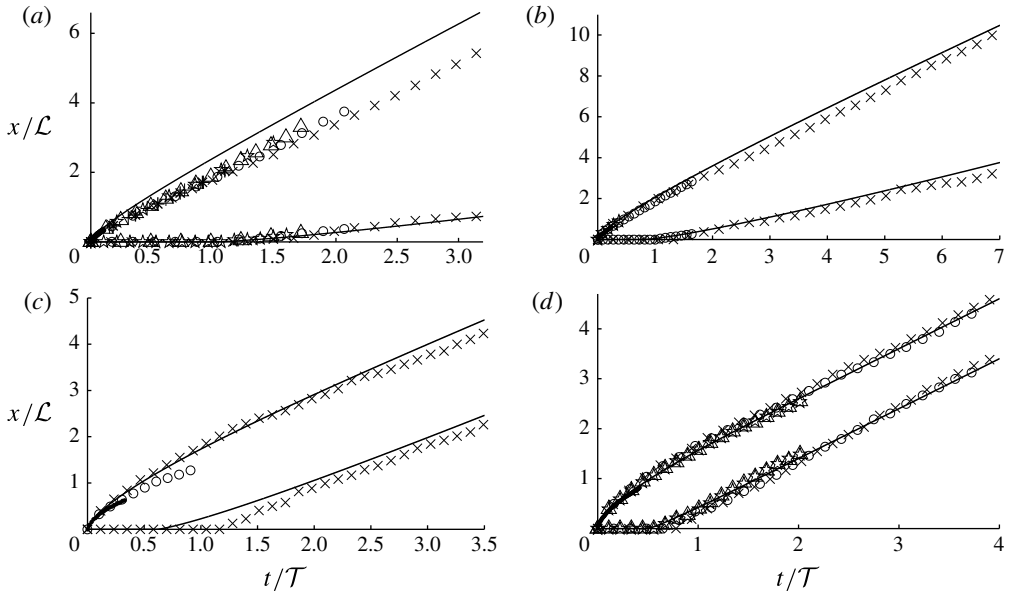

FIGURE 14. Comparison between our theoretical predictions (solid curves) and the experimental data for the evolution of the contact lines $X_U(t)$ and $X_L(t)$ gathered from the four sets of experiments (a)–(d), with the symbols listed in table 1.

At the In Salah test site, the density of carbon dioxide $\rho \approx 850$ kg m^{-3} and its viscosity $\mu \approx 8 \times 10^{-4}$ Pa s are both slightly larger than at Sleipner, owing to the higher pressures associated with its deeper injection (Vasco *et al.* 2010). The aquifer has a thickness of 20 m, with no separation into interstitial layers, and having the significantly smaller porosity $\phi \approx 0.15$ and permeability $k \approx 10^{-14}$ m^2 (Vasco *et al.* 2010). While the injection at Sleipner occurs at a single injection well, that at In Salah is achieved through three separate wells several kilometres apart. Assuming that the mean rate of injection 0.03 m^3 s^{-1} is roughly partitioned between the three wells, we estimate the characteristic volumetric fluxes through each as $Q \approx 0.01$ m^3 s^{-1}.

The injection of CO_2 at both sites is achieved through an effective point source at an injection well, near which the flow can be approximated as axisymmetric (Lyle *et al.* 2005; Nordbotten & Celia 2006; Bickle *et al.* 2007). Further downstream, the flows have been observed to form more elongated shapes (Bickle *et al.* 2007; Vasco *et al.* 2010; Boait *et al.* 2012). Using the satellite interferometric and seismic data provided by Vasco *et al.* (2010) and Boait *et al.* (2012) as reference, we infer that the horizontal extents of the largest CO_2 currents at In Salah and Sleipner are both characterized by $\mathscr{W} \approx 1$ km. As a representative calculation, we formulate the characteristic flux per unit width as $q_0 = Q/(2\mathscr{W})$, where Q is the volumetric flux of injection and the 2 has been included here to account for the partitioning of the flow at the source. With these parameter estimates, the intrinsic length and time scales (3.3*a*,*b*) can be evaluated as

$$\text{Sleipner:} \quad \mathscr{L} \approx 30 \text{ km}, \quad \mathscr{T} \approx 40 \text{ years}, \tag{5.1a,b}$$

$$\text{In Salah:} \quad \mathscr{L} \approx 0.1 \text{ km}, \quad \mathscr{T} \approx 3 \text{ years}, \tag{5.2a,b}$$

respectively. The estimates (5.1*a*,*b*) indicate that confinement has had only a moderate influence on the dynamics of the largest CO_2 currents at Sleipner and is consistent

with the injection pressure and buoyancy having played comparable roles. The much smaller length and time scales (5.2*a*,*b*) estimated for In Salah indicate that confinement has played a dominant role there soon after the initiation of the injection. The stark contrasts between the scales of (5.1*a*,*b*) and (5.2*a*,*b*) can be attributed almost entirely to the differences in porosity ϕ and permeability k between the two sites.

Analysis of geological samples has indicated that the permeability of the sandstone layer k at Sleipner can vary by up to a factor of three (Chadwick *et al.* 2004). Such heterogeneities introduce corresponding uncertainties in our characterization of the intrinsic length and time scales (5.1) and (5.2). Their effects may also introduce new fluid-mechanical phenomena not described by our model. Nevertheless, the application of our two-dimensional results can be expected to provide an illuminating, even if not complete, characterization of the intrinsic transitional scales on which confinement impacts the flow. In geophysical settings in which the current sustains an approximately circular shape downstream, as is evident for example in some of the horizons at Sleipner (Boait *et al.* 2012), an axisymmetric idealization may be more appropriate (Nordbotten & Celia 2006). For a more developed geophysical comparison, a theoretical model that can account for three-dimensional variations in topography and permeability is needed in order to describe in greater detail the more complex flows that can arise.

6. Conclusions

We have developed general equations describing flows in porous layers of constant depth and explored transitions between gravity-driven and injection-driven flows. A scaling analysis between terms in the governing equations reveals that the relative importance of the gravity-driven flow compared to the injection-driven flow is characterized by the dimensionless ratio $\widetilde{G} \equiv MH/h$, where M is the ratio of the viscosities between the two fluids. For $\widetilde{G} \gg 1$, the dynamics are dominated by gradients in hydrostatic pressure due to variations in the slope of the interface position. For $\widetilde{G} \ll 1$, the dynamics are instead dominated by the pressure gradients that arise due to the pressurization of the flow at the injection.

Our analysis of the injection into a two-dimensional horizontal aquifer showed that the flow transitions from a hydrostatically controlled regime at early times towards one of three different late-time regimes, depending on whether the mobility ratio M is greater than, equal to or less than unity. The time to transition away from the gravitationally controlled state was shown to increase cubically with the mobility ratio M.

If the injected fluid is less viscous ($M < 1$), as is relevant to the injection of CO_2 into saline aquifers, the spreading due to gradients in hydrostatic pressure ultimately becomes negligible, with the flow converging towards a similarity solution that is independent of the permeability of the medium. The positions of the contact lines approach asymptotes that each evolve linearly in time but with different prefactors, implying that the contact lines remain a significant distance apart, with the length of the interface continuing to stretch. As M decreases to zero, the time scale on which the position of the upper contact line approaches that predicted by the similarity solution decreases but that of the lower contact line increases as a consequence of significant buoyancy gradients persisting near the injection. A stability analysis of the similarity solution shows that perturbations to it retain the information associated with the shape of the initial perturbation but decay relatively to it as t^{-1}.

If the fluids have equal viscosities ($M = 1$), then both contact lines approach the same leading-order asymptotic position t. However, lateral expansion of the interface

occurs at the next order, growing as $t^{1/2}$ due to buoyancy-induced spreading, with the correction approaching a similarity solution in which the interface is linear. The dissipation due to buoyancy gradients causes perturbations to the similarity solution to lose information associated with the earlier transient flow, with perturbations decaying algebraically as t^{-1}.

If the viscosity of the injected fluid is greater than that of the ambient fluid ($M > 1$), then a similar leading-order linear growth of the contact lines emerges but with the interface position converging towards a steady state in a frame moving with the contact lines. At late times, the interface approaches a linear profile that becomes pushed forwards by newly injected fluid at constant speed. Perturbations to this state decay exponentially with time, with the flow again losing information of the earlier transient flow at a rate that increases with the mobility ratio M.

Illustrative estimates of the length and time scales indicate that the injection pressures due to the vertical confinement of the flow have a dominant influence on the dynamics of the CO_2 at In Salah and are less important, though not necessarily negligible, at Sleipner. The theoretical predictions for the positions of the interface and contact lines showed good agreement with data from a series of laboratory experiments.

Acknowledgements

This work was supported by the PANACEA collaborative project funded by the European Commission. We are grateful to Mark Hallworth, Colin Hitch and David Page-Croft for assistance in the preparation of our laboratory experiments. The research of J.A.N. is supported by a Royal Society University Research Fellowship. H.E.H. is partially supported by a Wolfson Royal Society merit award.

Appendix A. The transition towards horizontal flow

An idealized line source naturally leads to a localized radial flow of the form $u \sim u_R \equiv 4q_0/2\pi r$, where r is the distance from the source, implying that the theory of predominantly horizontal flow outlined in § 2 does not apply close to the source. This radial pressure gradient decays to the hydrostatic pressure gradient ($u_R \sim U$) once $x \sim \mathscr{D} \equiv q_0/\phi U$, indicating that the flow transitions to a region of predominantly horizontal flow over a horizontal distance of order $\mathscr{D}$ (Pegler *et al.* 2013*b*).

If the injected current fills the depth of the aquifer at the source before $x \sim \mathscr{D}$, then the transition to horizontal flow can be induced by the confinement of the flow. Specifically, once the current spans the depth of the medium, viscous stresses will dissipate any vertical pressure gradients imposed at the source over a horizontal distance of order H.

In general, a source distributed along the top, bottom or interior of the porous layer, or areally across its depth, can all be expected to lead to equivalent flows in the region $x \gg \min(H, \mathscr{D})$, with the information associated with the nature of the injection lost over a horizontal distance of order $\min(H, \mathscr{D})$. Which of buoyancy or confinement is the more influential effect in directing the flow to being horizontal can be measured by the dimensionless source strength $S \equiv \mathscr{D}/H$.

Appendix B. Asymptotic evolution with equal viscosities

Substituting perturbation expansions of the form $h = h_0(\xi) + h_1$, $Z_U = 1 + Z_{U,1}$ and $Z_L = -1 + Z_{L,1}$, where h_1, $Z_{U,1}$, $Z_{L,1} \ll 1$, into (3.29)–(3.31), and neglecting terms

quadratic in small quantities, we obtain the linearized equations

$$t\frac{\partial h_1}{\partial t} - \frac{1}{2}h_1 = \frac{1}{4}\frac{\partial}{\partial \zeta}\left[(1-\zeta^2)\frac{\partial h_1}{\partial \zeta}\right], \tag{B 1}$$

$$h_1 = Z_{U,1}/2, \quad t\dot{Z}_{U,1} + Z_{U,1}/2 = -\partial h_1/\partial\zeta \quad (\zeta = 1), \tag{B 2a,b}$$

$$h_1 = Z_{L,1}/2, \quad t\dot{Z}_{L,1} + Z_{L,1}/2 = \partial h_1/\partial\zeta \quad (\zeta = -1). \tag{B 3a,b}$$

Trying separable solutions of the form $h_1 = t^{-\alpha}\psi(\zeta)$, $Z_{U,1} = t^{-\alpha}\chi_U$ and $Z_{L,1} = t^{-\alpha}\chi_L$, where α is the exponent of decay, and χ_U and χ_L are constants representing the coordinates of the contact lines (cf. Grundy & McLaughlin 1982; Mathunjwa & Hogg 2006), in (B 1)–(B 3), we obtain the Sturm–Liouville eigenvalue problem

$$[(1-\zeta^2)\psi']' + 2(2\alpha - 1)\psi = 0, \tag{B.4}$$

$$\psi = \chi_U/2, \quad \left(-\alpha + \frac{1}{2}\right)\chi_U = -\psi' \quad (\zeta = 1), \tag{B 5a,b}$$

$$\psi = \chi_L/2, \quad \left(-\alpha + \frac{1}{2}\right)\chi_L = \psi' \quad (\zeta = -1). \tag{B 6a,b}$$

Eliminating χ_L and χ_U between (B 5a,b) and (B 6a,b), respectively, we obtain

$$(1-2\alpha)\psi = \mp\psi' \quad (\zeta = \pm 1), \tag{B 7}$$

which, when combined with (B 4), simply reduce to regularity conditions on ψ'' at $\zeta = \pm 1$. If we set $2(2\alpha - 1) = n(n+1)$ then these regularity conditions, along with (B 4), are together equivalent to the classical Sturm–Liouville eigenvalue problem associated with Legendre's equation (Abramowitz & Stegun 1972). This problem is solved by the polynomial eigenfunctions $\psi = P_n(\zeta)$ and eigenvalues $2(2\alpha - 1) = n(n+1)$, where $n = 1, 2, \ldots, \infty$ and P_n is the nth Legendre polynomial. At late times ($t \to \infty$), the leading-order contribution to h_1 is given by a constant multiple of the eigenmode $P_n(\zeta)$ associated with the smallest exponent of decay $\alpha(n)$. That occurs when $\alpha = n = 1$, implying that $h_1 \sim At^{-1}P_1(\zeta)$, where A is a constant, from which (3.34) follows on noting that $P_1 = \zeta$ is linear.

Appendix C. Asymptotic evolution with less viscous ambient fluid

Substituting perturbation expansions of the form $h = h_0 + h_1$, $u = 1 + u_1$, $X_U = t + l/2 + \Xi_{U,1}$ and $X_L = t - l/2 + \Xi_{L,1}$ into (3.35), (3.8) and (3.9), we obtain

$$\frac{\partial h}{\partial t} = -\frac{\partial}{\partial \zeta}(h_0 u_1), \quad u_1 = \frac{-M(1-h_0)}{h_0 + M(1-h_0)}\frac{\partial h_1}{\partial \zeta}, \tag{C 1a,b}$$

$$h_1 = \Xi_{U,1}/l, \quad \dot{\Xi}_{U,1} = u_1 = -\partial h_1/\partial\zeta \quad (\zeta = l), \tag{C 2a,b}$$

$$h_1 = \Xi_{L,1}/l, \quad \dot{\Xi}_{L,1} = u_1 = 0 \quad (\zeta = 0), \tag{C 3a,b}$$

where $\zeta \equiv \xi + l/2$ and $h_0(\zeta) = 1 - \zeta/l$ is the base state. Trying separable solutions of the form $h_1 = \mathrm{e}^{-\Lambda t}\psi(\zeta)$, where Λ is the exponent of decay, (C 1a,b) become

$$\Lambda\psi = [D(\zeta)\psi']', \quad \text{where } D(\zeta) \equiv \frac{-Mh_0(1-h_0)}{h_0 + M(1-h_0)}. \tag{C 4a,b}$$

The combination of (C 2) and (C 3) with (C 4*a*) implies the regularity of ψ at $\zeta = 0$ and l. Solving this Sturm–Liouville eigenvalue problem numerically using a fourth-order Runge–Kutta scheme, we obtain the values of the exponent of decay $\Lambda(M)$ plotted in figure 11 and the associated eigenfunctions $F_M(\xi)$ included in (3.40).

In the limit of inviscid ambient fluid $M \to \infty$, (C 4*a*) simplifies to

$$\Lambda\psi = [(1-\zeta)\psi']' \quad \text{and hence} \quad (r\psi')' + r\psi = 0 \tag{C 5a,b}$$

when recast in terms of the new variable $r \equiv 2[\Lambda(1-\zeta)]^{1/2}$, where a prime here denotes $\mathrm{d}/\mathrm{d}\zeta$ in (C 5*a*) and $\mathrm{d}/\mathrm{d}r$ in (C 5*b*). The transformed equation (C 5*b*) is Bessel's equation of order zero, which has the solution $\psi = \mathrm{J}_0(r)$ subject to the regularity condition at $r = 0$, where J_0 is the Bessel function of order zero. Substituting this solution into the integration of (C 5*b*) between the boundaries of the domain $r = 0$ and $2\sqrt{\Lambda}$, we obtain

$$\int_0^{2\sqrt{\Lambda}} r\psi \,\mathrm{d}r = \int_0^{2\sqrt{\Lambda}} rJ_0 \,\mathrm{d}r = [r\mathrm{J}_1]_0^{2\sqrt{\Lambda}} = 0 \quad \text{and hence} \quad \Lambda = j_1^2/4 \approx 3.67, \tag{C.6}$$

where J_1 is the Bessel function of order one and $j_1 \approx 3.83$ is its first positive zero. The value of Λ given by (C 6), shown by the thin dashed line in figure 11, describes the asymptotic exponent of decay as $M \to \infty$.

In the limit in which the injected fluid is only slightly more viscous than the ambient fluid $M \to 1^+$, (C 4*a*) simplifies to

$$[(1-s^2)\psi']' + l^2\Lambda\psi = 0, \tag{C.7}$$

where $s \equiv l\xi/2$ and we have used a prime here to denote $\mathrm{d}/\mathrm{d}s$. If we write $l^2\Lambda \equiv n(n+1)$, where n is a constant, then (C 7) reads as Legendre's equation, which, as recalled in appendix B, has its smallest positive eigenvalue when $n = 1$ and $\psi = P_1 = \zeta$. The exponent of decay $\Lambda = 2l^{-2} \sim 2(M-1)^2$ for $n = 1$, shown by the thick dashed curve in figure 11, describes the asymptotic value of Λ when M is greater than but close to unity.

REFERENCES

Abramowitz, M. & Stegun, I. A. 1972 *Handbook of Mathematical Functions with Formulas, Graphs, and Mathematical Tables*. Dover.

Acton, J. M., Huppert, H. E. & Worster, M. G. 2001 Two-dimensional viscous gravity currents flowing over a deep porous medium. *J. Fluid Mech.* **440**, 359–380.

Barenblatt, G. I. 1996 *Scaling, Self-Similarity, and Intermediate Asymptotics*. Cambridge University Press.

Bear, J. 1988 *Dynamics of Fluids in Porous Media*. Dover.

Bickle, M. J., Chadwick, R. A., Huppert, H. E., Hallworth, M. A. & Lyle, S. 2007 Modelling carbon dioxide accumulation at Sleipner: implications for underground carbon storage. *Earth Planet. Sci. Lett.* **255**, 164–176.

Boait, F. C., White, N. J., Bickle, M. J., Chadwick, R. A., Neufeld, J. A. & Huppert, H. E. 2012 Spatial and temporal evolution of injected CO_2 at the Sleipner field, North Sea. *J. Geophys. Res.* **117**, B03309.

CHADWICK, R. A., ZWEIGEL, P., GREGERSEN, U., KIRBY, G. A., HOLLOWAY, S. & JOHANNESSEN, P. N. 2004 Geological reservoir characterization of a CO_2 storage site: the Utsira Sand, Sleipner, northern North Sea. *Energy* **29**, 1371–1381.

DAKE, L. P. 2010 *Fundamentals of Reservoir Engineering*. *(Developments in Petroleum Science)*, vol. 8. Elsevier.

GOLDING, M. J. & HUPPERT, H. E. 2010 The effect of confining impermeable boundaries on gravity currents in a porous medium. *J. Fluid Mech.* **649**, 1–17.

GRUNDY, R. E. & MCLAUGHLIN, R. 1982 Eigenvalues of the Barenblatt–Pattle similarity solution in nonlinear diffusion. *Proc. R. Soc. Lond.* A **649**, 89–100.

GUNN, I. & WOODS, A. W. 2011 On the flow of buoyant fluid injected into a confined, inclined aquifer. *J. Fluid Mech.* **672**, 109–129.

GUNN, I. & WOODS, A. W. 2012 On the flow of buoyant fluid injected into an aquifer with a background flow. *J. Fluid Mech.* **706**, 274–294.

HESSE, M. A., ORR JR, F. M. & TCHELEPI, H. A. 2008 Gravity currents with residual trapping. *J. Fluid Mech.* **611**, 35–60.

HESSE, M. A., TCHELEPI, H. A., CANTWELL, B. J. & ORR JR., F. M. 2007 Gravity currents in horizontal porous layers: transition from early to late self-similarity. *J. Fluid Mech.* **577**, 363–383.

HUPPERT, H. E. 1986 The intrusion of fluid mechanics into geology. *J. Fluid Mech.* **173**, 557–594.

HUPPERT, H. E. & WOODS, A. W. 1995 Gravity-driven flows in porous layers. *J. Fluid Mech.* **292**, 55–69.

LYLE, S., HUPPERT, H. E., HALLWORTH, M., BICKLE, M. & CHADWICK, A. 2005 Axisymmetric gravity currents in a porous medium. *J. Fluid Mech.* **543**, 293–302.

MACMINN, C. W. & JUANES, R. 2009 Post-injection spreading and trapping of CO_2 in saline aquifers: impact of the plume shape at the end of injection. *Comput. Geosci.* **13**, 480–491.

MACMINN, C. W., SZULCZEWSKI, M. L. & JUANES, R. 2010 CO_2 migration in saline aquifers. Part 1: Capillary trapping under slope and groundwater flow. *J. Fluid Mech.* **662**, 329–351.

MACMINN, C. W., SZULCZEWSKI, M. L. & JUANES, R. 2011 CO_2 migration in saline aquifers. Part 2: Combined capillary and solubility trapping. *J. Fluid Mech.* **688**, 321–351.

MATHUNJWA, J. S. & HOGG, A. J. 2006 Self-similar gravity currents in porous media: linear stability of the Barenblatt–Pattle solution revisited. *Eur. J. Mech. (*B*/Fluids)* **25**, 360–378.

NORDBOTTEN, J. M. & CELIA, M. A. 2006 Similarity solutions for fluid injection into confined aquifers. *J. Fluid Mech.* **561**, 307–327.

ORR JR., F. M. 2009 Onshore geological storage of CO_2. *Science* **325**, 1656–1658.

PEGLER, S. S., HUPPERT, H. E. & NEUFELD, J. A. 2013*a* Topographic controls on gravity currents in porous media. *J. Fluid Mech.* **734**, 317–337.

PEGLER, S. S., KOWAL, K. N., HASENCLEVER, L. Q. & WORSTER, M. G. 2013*b* Lateral controls on grounding-line dynamics. *J. Fluid Mech.* **722**, R1.

PEGLER, S. S., LISTER, J. R. & WORSTER, M. G. 2012 Release of a viscous power-law fluid over an inviscid ocean. *J. Fluid Mech.* **700**, 261–281.

SAFFMAN, P. G. & TAYLOR, G. I. 1958 The penetration of a fluid into a porous medium or Hele-Shaw cell containing a more viscous liquid. *Proc. R. Soc. Lond.* A **245**, 312–329.

TAYLOR, G. I. 1953 Dispersion of soluble matter in solvent flowing slowly through a tube. *Proc. R. Soc. Lond.* A **219**, 186–203.

VASCO, D. W., RUCCI, A., FERRETTI, A., NOVALI, F., BISSELL, R. C., RINGROSE, P. S., MATHIESON, A. S. & WRIGHT, I. W. 2010 Satellite-based measurements of surface deformation reveal fluid flow associated with the geological storage of carbon dioxide. *Geophys. Res. Lett.* **37**, L03303.

VELLA, D. & HUPPERT, H. E. 2006 Gravity currents in a porous medium at an inclined plane. *J. Fluid Mech.* **555**, 353–362.

WOODS, A. W. & MASON, R. 2000 The dynamics of two-layer gravity-driven flows in permeable rock. *J. Fluid Mech.* **421**, 83–114.